A novel approach to separate absorption, refraction and scattering in analyzer based lung imaging

Queries for the author

Please reply to the following queries using the appropriate tool "SEND PROOFS" at the bottom of the preprint page on https://jinst.sissa.it

1. Please note that, following the JINST style, equations have been numbered following a section-specific numbering.

   References in the text have been consistently updated. Please check.

2. Please note that we have updated the information for ref. [11] according to the article's web page. Please check.

Jinst

Published by IOP Publishing for Sissa Medialab

Received: *December 20, 2019*
Revised: *March 19, 2020*
Accepted: *April 5, 2020*
Published: *???, 2020*

21st International Workshop on Radiation Imaging Detectors
7–12 July 2019
Crete, Greece

A novel approach to separate absorption, refraction and scattering in analyzer based lung imaging

R.H. Menk,[a,b,d,1] **L. Rigon,**[b,c] **L. Brombal,**[c] **S. Donato,**[c,e] **C. Petris**[c] **and F. Arfelli,**[b,c]

[a] *ELETTRA Sincrotrone Trieste, Trieste (TS), Italy*
[b] *INFN section of Trieste, Trieste (TS), Italy*
[c] *University of Trieste, Trieste (TS), Italy*
[d] *Department of Medical Imaging, University of Saskatchewan, Saskatoon, SK S7N 5A2, Canada*
[e] *University of Calabria, Arcavacata di Rende (CS), Italy*

E-mail: ralf.menk@elettra.eu

Abstract: In analyzer based imaging (ABI) scattering can be efficiently separated from refraction and absorption effects by acquiring three images of the sample. In the scattering image the lungs appear as areas of high intensity signal (area contrast), which is modulated by the local thickness of the scattering tissue intersecting the X-ray path. The scattering signal is also included in the so-called apparent absorption image, where it adds to the absorption contrast thanks to the extinction of rays which are deviated outside the analyzer crystal's acceptance window. The presence of scattering can be emphasized in the ratio between two images acquired with a strongly detuned and a perfectly tuned analyzer crystal, respectively: we name this ratio as the amplified scatter image. In this paper we present ABI scattering methods applied to postmortem mouse lung imaging to assess their diagnostic value. For this purpose images have been acquired at the SYRMEP beamline of the ELETTRA synchrotron in Trieste (Italy) with the Argus time delay integration CCD detector at a photon energy of 25 keV. Subsequently the parametric images, including the amplified scatter image have been obtained, and contrast and signal-to-noise ratio have been evaluated. It is noteworthy that images have been acquired with a radiation dose of some mGy, thus are compatible with dose restricted medical imaging settings such as mammography.

Keywords: Medical-image reconstruction methods and algorithms, computer-aided software; X-ray radiography and digital radiography (DR); X-ray monochromators; X-ray detectors

[1] Corresponding author.

https://doi.org/xxxxxxx

Contents

1 Introduction

One of the advantages of phase contrast X-ray imaging with respect to conventional X-ray attenuation is its capability of extracting complementary and useful physical properties of the sample under investigation. Different phase contrast methods have been developed and extensively applied at synchrotron radiation sources, one of them being Analyzer Based X-ray Imaging (ABI) [1], which utilizes perfect crystals exploring the X-ray deviation by their interaction with the sample. Such systems rely on the fact that for small phase gradients the refraction angle $\Delta\theta_R$ of X-rays can be expressed as $\Delta\theta_R = \frac{1}{k}\frac{\partial\phi(y)}{\partial y}$ where k is the length of the wave vector of the incident radiation and the second term on the right hand side is the first derivative of the phase in the diffraction direction y. Owing to the narrow angular acceptance of the analyzer a single image acquisition is sufficient to obtain qualitative and high signal to background radiographs, however, it requires multiple image acquisition schemes to assess quantitative metrics. ABI may yield three parametric output images [2–7], which assess different physical properties namely apparent absorption, refraction and scattering linked to dark field images, when a minimum of three input images are acquired and dedicated image processing on a pixel basis is applied. These modalities can be extended from planar images to computed tomography [8] and allow quantitatively retrieving of scattering even for wide scattering distribution. Linking the (sub) micro-structure to morphological changes in soft tissues at biocompatible radiation doses is a yet challenging problem due to the lack of quantitative characterization tools possessing sufficient structural sensitivity at this length scale. In this view dark field or scattering based images yielded by ABI possess additional valuable information on the microscopic range without necessarily employing a high-resolution imaging detector. ABI enables to qualitatively assess such scattering in a wide angular validity range. For biological samples this in turn might yield information on biological function in micrometer sized particulate systems as found for instance in lungs or as found in ultra sound μ-bubble contrast agents [9]. While the potential benefits of dark field and scattering images in lung imaging yielded with different phase contrast modalities are generally acknowledged [10], it is still in question for ABI, which image (single shot images, a linear combination of those or parametric images (i.e. the scatter image)) would provide the highest diagnostic value.

For this purpose contrast and signal-to-noise ratio in several regions of interest have been evaluated in post mortem analyzer based images of mice lungs, which were acquired at the SYRMEP beamline of the ELETTRA synchrotron in Trieste (Italy). For retrieving quantitative metrics of the parametric images the so-called G^{2}DEI algorithm [4] has been applied in this study.

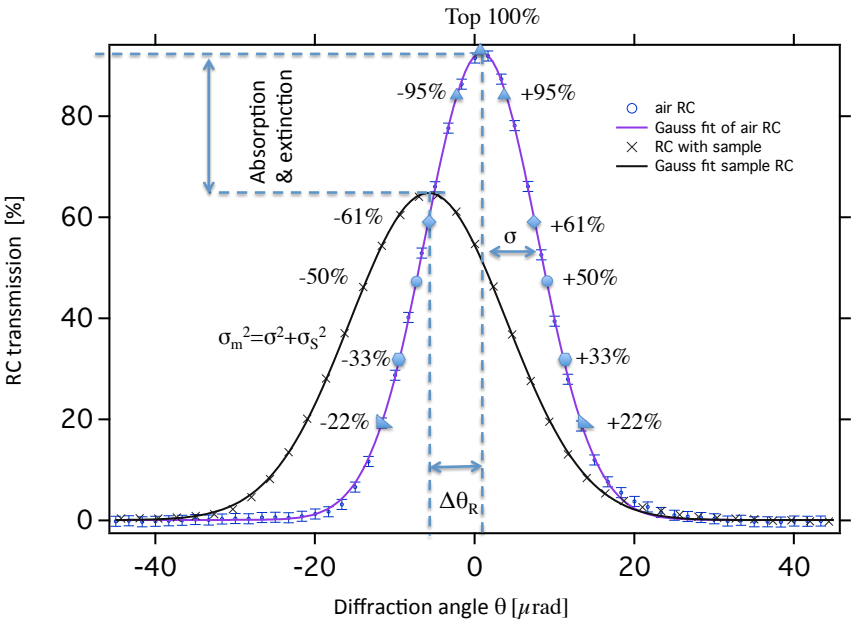

Figure 1. Reflectivity curve of the analyzer with and without sample in place.

In brief the G^{2}DEI algorithm traces back to the observation that an experimental transmission function of the analyzer crystal $R(\theta)$ versus the diffraction angle θ (the so-called rocking curve (RC) see figure 1) in absence of a sample can be approximated with reasonable fidelity by a Gaussian function, which is centered around its Bragg angle θ_B and possesses a standard deviation σ. Such experimental transmission function is a convolution of the intrinsic crystal reflectivity curves of the monochromator and the analyzer. Each of these curves features a Darwin width w_D and σ is proportional to w_D [11].

In the presence of an object upstream the analyzer the measured RC in a detector pixel is modulated according to the local absorption, refraction and scattering properties of the sample. In the presence of absorption the amplitude of the local RC is reduced, while refraction would generate a shift of the mean value by $\Delta\theta_R$. In the presence of Gaussian scattering with standard deviation σ_S the measured standard deviation σ_m of the local RC increases (thus $\sigma_m^2 = \sigma^2 + \sigma_S^2$) while the amplitude is reduced accordingly (extinction). If the analyzer is tuned to a specific angle θ_i then the measured intensity in presences of absorption, diffraction and scattering effects at that angle is according to [4] given by

$$I(\theta_i) = I_R \cdot \sqrt{\frac{\sigma^2}{\sigma_S^2 + \sigma^2}} \cdot \exp\left(-\frac{(\theta_i + \Delta\theta_R)^2}{2 \cdot (\sigma_S^2 + \sigma^2)}\right) \tag{1.1}$$

Equation 1.1 contains three unknowns, namely the apparent absorption I_R, the refraction angle $\Delta\theta_R$ and the width σ_S of the small angle scattering distribution. Recording a minimum of three images $I(\theta_i)$ at three different angular positions θ_i with $i = 1, 2, 3$ allows to solve for these unknowns on a pixel to pixel basis utilizing for instance the G^{2}DEI algorithm.

It is noteworthy that the apparent absorption I_R possesses the quantitative attenuation and the so-called extinction contrast i.e. the rejection of X-ray scattering, which is not transmitted by the analyzer. The apparent absorption image is obtained by inverting equation (1.1) and given by

$$I_R = I(\theta_i) \cdot \sqrt{\frac{\sigma_S^2 + \sigma^2}{\sigma^2}} \cdot \exp\left(\frac{(\theta_i + \Delta\theta_R)^2}{2 \cdot (\sigma_S^2 + \sigma^2)}\right) \tag{1.2}$$

Applying G^{2}DEI the refraction image $\Delta\theta_R$ is given by

$$\Delta\theta_R = \frac{\ln\left(\frac{I(\theta_3)}{I(\theta_2)}\right) \cdot (\theta_2^2 - \theta_1^2) - \ln\left(\frac{I(\theta_1)}{I(\theta_2)}\right) \cdot (\theta_2^2 - \theta_3^2)}{2 \cdot \left[\ln\left(\frac{I(\theta_1)}{I(\theta_2)}\right) \cdot (\theta_2 - \theta_3) - \ln\left(\frac{I(\theta_3)}{I(\theta_2)}\right) \cdot (\theta_2 - \theta_1)\right]} \tag{1.3}$$

and represents a quantitative map of the refraction angles. In other words the pixel values reflect the average deviation angle of X-rays from their original path. In contrast pixel values in the scattering or dark field image σ_S, which is given by

$$\sigma_S^2 = \frac{(\theta_2 - \theta_1) \cdot (\theta_2 - \theta_3) \cdot (\theta_1 - \theta_3)}{2 \cdot \left[\ln\left(\frac{I(\theta_1)}{I(\theta_2)}\right) \cdot (\theta_2 - \theta_3) - \ln\left(\frac{I(\theta_3)}{I(\theta_2)}\right) \cdot (\theta_2 - \theta_1)\right]} - \sigma^2 \tag{1.4}$$

represents the standard derivation of the scattering distribution in that pixel.

In images $I(\theta_f)$, which have been acquired with a strongly detuned analyzer at an angle $|\theta_f - \theta_B| \geq \sigma$ direct radiation is substantially suppressed while scattered radiation is effectively collected on the imaging detector. Although this method yields high signal-to-noise dark field or scattering images a quantitative metrics is not provided in this case. However, the signal-to-noise ratio of this dark field image can be further enhanced by normalising $I(\theta_f)$ to an image $I(\theta_B)$, which has been acquired at the peak of the reflectivity curve. In the resulting amplified scatter image

$$\eta = I(\theta_f)/I(\theta_B) \tag{1.5}$$

absorption effects are equalised while the extinction effect intensifies scattering at the same time.

In this study single images acquired at different angular positions of the analyzer reflectivity curve (figure 1) as well as the parametric G^{2}DEI images (equations (1.2))–(1.4) and the amplified scatter image (equation (1.5)) have been analyzed.

2 Materials and methods

All measurements have been carried out at the SYRMEP bending magnet beamline at the ELETTRA synchrotron light source in Trieste (Italy) [12]. The optics of the SYRMEP beamline (figure 2) features a double crystal Si(1,1,1) monochromator, utilized in the symmetric Bragg configuration. The monochromator spans an energy range from 8.5 keV to 40 keV and is placed in vacuum.

Sample, analyzer crystal and detector are located in air in the experimental hutch downstream of the monochromator at 23 m, 23.5 m and 24 m, respectively. At the sample position the maximum available cross section of the monochromatic, laminar X-ray beam is 150 mm in width and about 4 mm (FWHM) in height, which can be reduced by means of two micrometric slit systems upstream the sample. Sample and detector are placed on micrometric stages, allowing simultaneous vertical scanning through the beam and thus the acquisition of two-dimensional planar images. In addition a rotational stage allows the rotation of the sample for acquiring tomographic data sets.

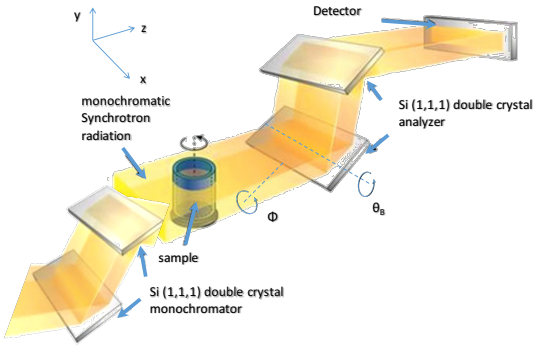

Figure 2. Scheme of the setup.

The analyzer comprising of two perfect Si(1,1,1) crystals can be rotated around the Bragg angle θ_B with a nominal precision of 0.15 µrad utilizing a Piezo drive (P-840 Preloaded Piezo Actuators, from Physik Instrumente (PI) GmbH & Co. KG, Karlsruhe, Germany). The analyzer stage is fixed onto an optical table and mechanically decoupled from the other movement stages minimising mechanical vibrations. The detector was an ARGUS CCD detector, which features a columnar CsI scintillator and has been provided by Teledyne DALSA (Ontario, Canada). This high quantum efficiency detector is normally applied in clinical mammography, panoramic dental imaging and general radiography applications. The field of view is about 220 (h) mm · 6.9 (v) mm with an effective pixel size of 54 µm · 54 µm for a pixel binning of 2, which was used during data acquisition. For planar images the ARGUS CCD was operated in time delay integration mode. Typically the line rate was set to 200 lines/s, the scan range was 100 mm and the scan velocity was 10 mm/s. All acquired images have been pedestal and flat field corrected using the IDL package (Harris Geospatial solutions, Exelis Visual Information Solutions, Broomfield, U.S.A.) before applying the G^{2}DEI algorithm. The parametric images have been retrieved using IDL, which applies the G^{2}DEI algorithm. The IDL package and the Fiji package [13] have been used for further image processing and image analysis.

During data acquisition two in-situ ionisation chambers (not shown in figure 2), one placed upstream of the sample and the second one downstream of the analyzer have been used to monitor in real time the reflectivity of the analyzer, thus the diffraction angle θ. Single images have been acquired typically at the low and high angle side at 5%, 10%, 50% and at 100% of the maximum reflectivity of the analyzer. A triad of images acquired at ±50% and 100% has been used for the G^{2}DEI algorithm while two images acquired at the ±5% or ±10% and 100% have been utilized to calculate the amplified scatter image η.

For the determination of the contrast (C) and the signal-to-noise ratio (SNR) regions of interest (ROIs) have been identified as indicated in a planar scattering image (figure 3) and have been propagated throughout all the other single and parametric images.

The animal experiments described here were carried out in accordance with the European directive (86/609/CE — 1986) for animal trials and the ethics committee of the University of Trieste approved the study.

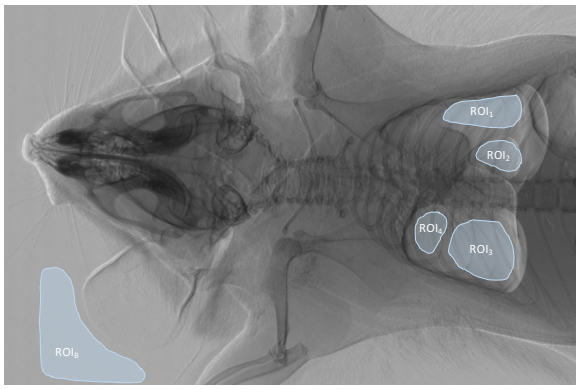

Figure 3. Selected regions of interest depicted within the torso of a mouse. One additional ROI is chosen in the background. The image was acquired at the low angle at 50% of the peak intensity.

Of interest for the study at hand are those ROIs indicated with 1–4 and their associated background $\mathrm{ROI_B}$ (left). Due to the different volume of the lobes the contrast and SNR have been identified for the left and the right lung separately. For this reason the mean values $\langle m\rangle_{\mathrm{ROI}}$ of $\mathrm{ROI_1}$ and $\mathrm{ROI_2}$ and $\mathrm{ROI_3}$ and $\mathrm{ROI_4}$, respectively, have been combined. Together with the mean $\langle m\rangle_{\mathrm{B}}$ in the background the contrast was calculated according to its standard definition as

$$C = \left| \frac{\langle m\rangle_{\mathrm{B}} - \langle m\rangle_{\mathrm{ROI}}}{\langle m\rangle_{\mathrm{B}}} \right| \tag{2.1}$$

and subsequently together with the standard error σ_{B} of the mean in the $\mathrm{ROI_B}$

$$\mathrm{SNR} = \left| \frac{\langle m\rangle_{\mathrm{B}} - \langle m\rangle_{\mathrm{ROI}}}{\sigma_{\mathrm{B}}} \right| \tag{2.2}$$

It is worth to notice that in equation (2.1) and equation (2.2) the modulus was used in order to avoid zero crossings when comparing extinction and dark field contrast / SNR, respectively. The standard error σ_{B} of the mean in the background thus the flat image was used to account for Poisson noise only and not for the superimposed structural noise stemming from the lung morphology. It is noteworthy, that the standard errors for the contrast and the signal-to-noise ratio as quoted in table 1 have been derived by error propagation utilizing σ_{B}.

3 Results

Postmortem parametric images of a mouse torso acquired at 25 keV photon energy are presented in figure 4. The transmission in the apparent absorption image (figure 4a) ranges from 10%–90%.

Visible in the refraction image (figure 4b), in which the displayed angles are ranging from −12 µrad to +12 µrad, is the trachea branching into two bronchi. The right bronchus bifurcates close to the middle and inferior lobes. Superior lobe and post-caval lobe as well as signatures from the annular cartilaginous ligaments of trachea and bronchi can be appreciated to a certain extent.

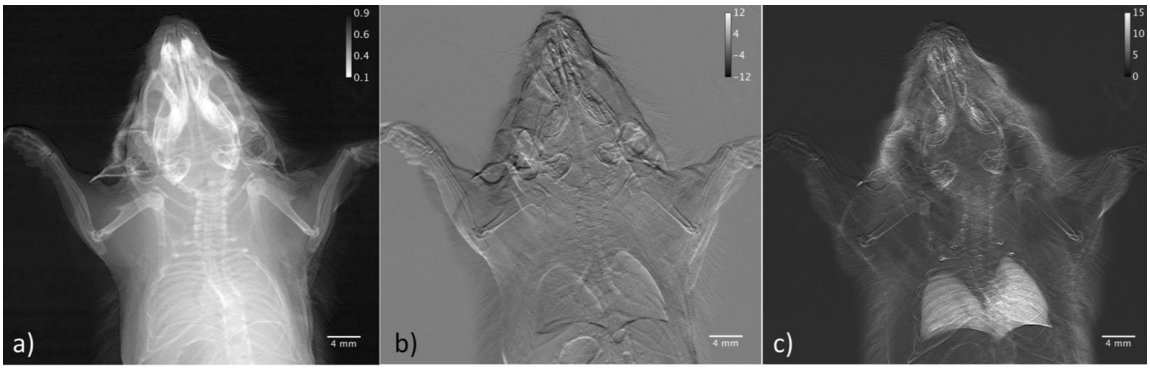

Figure 4. The three parametric images acquired at 25 keV and obtained by applying the G^{2}DEI algorithm. a) the apparent absorption image (*ApAb*), b) the refraction image and c) the scattering image.

The boundaries of the pleura give raise to refraction, which is in the order of −5 µrad and +5 µrad for the low-angle and high-angle side. In the scattering image (figure 4c) the lungs appear as areas of high intensity signal (area contrast), which is modulated by local thickness of the organ and thus by the number of alveoli intersecting the X-ray path. The scattering widths displayed in the scattering image are ranging from 0 µrad (black) to 15 µrad (white) whereas the average in the right lobe is 10 µrad (standard deviation = 1.5 µrad), in the upper part of the superior lobe 7.9 µrad (standard deviation = 1.0 µrad) and 11.5 µrad (standard deviation = 1.1 µrad) in the lower part of the inferior lobe. The average value in the left lobe is 8.8 µrad with a standard deviation of 1.2 µrad.

Indicated in table 1 are the yielded contrast and the *SNR* with respect to the flat field obtained from the ROIs as indicated in figure 3 versus the respective planar image type for two different mice. Single images have been acquired with the Argus detector at a photon energy of 25 keV and subsequently the parametric images and the amplified scatter image have been obtained as described previously. Due to the different volume of the lobes, two rows indicating the contrast and the SNR, respectively, are used for each mouse lung in this table. The first 3 columns of table 1 represent the finding in single images recorded at angles associated with the indicated reflectivity thus at low 10%, low 50% and on the peak of the analyzer's reflectivity curve. The next three columns represent the parametric images as yielded by the G^{2}DEI algorithm. In particular *ApAb* represents the apparent absorption image (equation (1.2)), *Scatter* the scattering image according to equation (1.4), thus the standard derivation of the measured scattering distribution and *amp. scat. image* represents the amplified scatter image (η), defined in equation (1.5).

For the single images the contrast is increasing with decreasing absolute Bragg angle and approximately unity for the peak image, which is not surprising since here the increasing extinction governs the contrast. This is also the reason why the image acquired at the peak of the reflectivity curve features a 20% higher contrast than the apparent absorption image. Not unexpected the highest contrast of 390 ± 5 and 432 ± 6 is observed for right lungs of the two mice in the parametric

Table 1. Contrast and *SNR* against air for two mice.

	low 10%	low 50%	peak	ApAb	Scatter	amp. scat. image
Contrast mouse 1 right lung	0.779 ± 0.008	0.93 ± 0.02	0.959± 0.002	0.77 ± 0.02	432 ± 6	10.36 ± 0.02
Contrast mouse 1 left lung	0.84 ± 0.05	0.95 ± 0.01	0.973 ± 0.007	0.772 ± 0.001	376 ± 5	9.11 ± 0.02
SNR mouse 1 right lung	5353 ± 8	10988 ± 35	10412 ± 37	8225 ± 25	10643 ± 21	27266 ± 53
SNR mouse 1 left lung	5351 ± 10	8749 ± 21	8701 ± 19	6873 ± 54	9540 ± 13	32516 ± 68
Contrast mouse 2 right lung	0.827 ± 0.009	0.94 ± 0.02	0.96 ± 0.01	0.71 ± 0.02	390 ± 5	8.12 ± 0.04
Contrast mouse 2 left lung	0.87 ± 0.05	0.96 ± 0.02	0.976 ± 0.001	0.78 ± 0.01	345 ± 4	6.75 ± 0.02
SNR mouse 2 right lung	3703 ± 6	8365 ± 29	7234 ± 14	5714 ± 41	5701 ± 10	27265 ± 53
SNR mouse 2 left lung	3192 ± 9	6668 ± 19	7110 ± 15	5616 ± 59	5067 ± 12	23690 ± 52

scattering images (equation (1.4)). This high contrast is due to the fact that in the scattering image each photon is effectively collected, thus a high signal in comparison to the null background is yielded. It is noteworthy that a somewhat lower contrast of 345 ± 4 and 376 ± 5 in the left lungs of the animals have been found. Keeping in mind the small error-bars these differences are significant and are due to the different numbers of alveoli, thus the number of scatters in the different lobes. The same arguments are in principle valid for the amplified scattering images η calculated according equation (1.5) and one would expect a similar contrast as in the scatter image. However, as in the case of the far angle images also in here a certain pedestal > 0 is always present in the η image that compromises the contrast accordingly.

For the *SNR* the single images especially the peak and those acquired at the 50% feature high *SNRs* between 8000 and 11000 for the left and right lobe of mouse 1 and a somewhat lower *SNR* (7110 ± 15 and 7234 ± 14) for the second animal. Since in the Poisson case the signal-to-noise ratio increases with the square root of the measured photons this causes for high intensity images such as the peak image the observed and elevated *SNR*. As extinction contrast is mostly removed and the image noise is increased by at least by $\sqrt{3}$ in the apparent absorption image (*ApAb*) the *SNR* here is lower than that in the associated peak image. The *SNRs* in the parametric scattering image are as high as in the peak image for the first animal and in the same order as the *SNR* of the apparent absorption image for the second mouse. An explanation for this behaviour is still missing and it would require more statistics using additional animals. Eventually, the combination of high contrast and low relative noise in the background of the amplified scatter image leads to the observed increase in the *SNR* of ≥ 20000, which is superior to that of the peak image.

4 Conclusion and outlook

The study discussed here showed that the highest contrast (against an air background) is obtained in the parametric scattering image, which has been yielded by applying the G^{2}DEI algorithm utilizing a triad of single shot images at ± 50% and 100% of the analyzer's reflectivity curve. Typically the contrast obtained in this image outstrips the contrast in single shot images by almost two orders of magnitude. Unfortunately this predominance in contrast is not propagated into a superior *SNR*, which is due to a higher background noise when compared to single shot or the apparent absorption image. The amplified scattering image η features the highest signal-to-noise ratio of some ten thousands. As stated before the apparent absorption image provides a quantitative metrics, while the amplified scattering image yields only qualitative data. It is noteworthy that the single shot images have been acquired with a radiation dose of some mGy, thus are compatible with radiation

dose for restricted medical imaging settings such as mammography. The contrast of the parametric scattering image is very sensitive to the number of scatterers, which are intersected by the ray path and thus to the organ thickness. The studies here implied that the sensitivity is in the order of some scatterers, thus some alveoli. This means lung pathologies on the µm level can be imaged with a bio compatible radiation dose. Further investigations targeting also different pixel sizes are carried out at the time being. In the next steps in-vivo trials are envisaged in animal models of human diseases.

References

[1] D. Chapman, W. Thomlinson, R.E. Johnston, D. Washburn, E. Pisano, N. Gmür et al., *Diffraction enhanced x-ray imaging*, *Phys. Med. Biol.* **42** (1997) 2015.

[2] L. Rigon, H.-J. Besch, F. Arfelli, R.-H. Menk, G. Heitner and H. Plothow-Besch, *A new DEI algorithm capable of investigating sub-pixel structures*, *J. Phys.* **D 36** (2003) A107.

[3] L. Rigon, F. Arfelli and R.-H. Menk, *Generalized diffraction enhanced imaging to retrieve absorption, refraction and scattering effects*, *J. Phys.* **D 40** (2007) 3077.

[4] F. Arfelli, A. Astolfo, L. Rigon and R.H. Menk, *A gaussian extension for diffraction enhanced imaging*, *Sci. Rep.* **8** (2018) 362.

[5] M.N. Wernick, O. Wirjadi, D. Chapman, Z. Zhong, N.P. Galatsanos, Y. Yang et al., *Multiple-image radiography*, *Phys. Med. Biol.* **48** (2003) 3875.

[6] E. Pagot, P. Cloetens, S. Fiedler, A. Bravin, P. Coan, J. Baruchel et al., *A method to extract quantitative information in analyzer-based x-ray phase contrast imaging*, *Appl. Phys. Lett.* **82** (2003) 3421.

[7] O. Oltulu, Z. Zhong, M. Hasnah, M.N. Wernick and D. Chapman, *Extraction of extinction, refraction and absorption properties in diffraction enhanced imaging*, *J. Phys.* **D 36** (2003) 2152.

[8] L. Rigon, A. Astolfo, F. Arfelli and R.-H. Menk, *Generalized diffraction enhanced imaging: Application to tomography*, *Eur. J. Radiol.* **68** (2008) S3.

[9] F. Arfelli, L. Rigon and R.H. Menk, *Microbubbles as x-ray scattering contrast agents using analyzer-based imaging*, *Phys. Med. Biol.* **55** (2010) 1643.

[10] A. Yaroshenko, T. Pritzke, M. Koschlig, N. Kamgari, K. Willer, L. Gromann et al., *Visualization of neonatal lung injury associated with mechanical ventilation using x-ray dark-field radiography*, *Sci. Rep.* **6** (2016) 24269.

[11] C.G. Darwin, *The theory of X-ray reflexion*, *Phil. Mag.* **27** (1914) 315.

[12] A. Abrami, F. Arfelli, R. Barroso, A. Bergamaschi, F. Billè, P. Bregant et al., *Medical applications of synchrotron radiation at the SYRMEP beamline of ELETTRA*, *Nucl. Instrum. Meth.* **A 548** (2005) 221.

[13] J. Schindelin, I. Arganda-Carreras, E. Frise, V. Kaynig, M. Longair, T. Pietzsch et al., *Fiji: an open-source platform for biological-image analysis*, *Nat. Meth.* **9** (2012) 676.